

The Anti-proliferative Activity of Factory Wastes Nanoparticles against Uterus Cancer Cells: In-vitro Study

Nadia Jasim Ghdeeb¹✉, Asmaa Hadi Mohammed¹, Aseel Mustafa Abdul Majeed²

¹Department Of Physics, Baghdad, College Of Science, Mustansyriah University, Iraq.

²Department of Physics, College of Science, Al-Nahrain University, Baghdad, Iraq.

✉ Corresponding author. E-mail: nadiajasim127@uomustansiriyah.edu.iq

Received: Feb. 26, 2022; **Accepted:** Sep. 19, 2022; **Published:** Oct. 21, 2022

Citation: Nadia Jasim Ghdeeb, Asmaa Hadi Mohammed, and Aseel Mustafa Abdul Majeed, The Anti-proliferative Activity of Factory Wastes Nanoparticles against Uterus Cancer Cells: In-vitro Study. *Nano Biomed. Eng.*, 2022, 14(2): 149-158.

DOI: 10.5101/nbe.v14i2.p149-158.

Abstract

As a result of increasingly rigorous environmental legislation and industry adoption of waste minimization recommendations, the development of recycling and reuse possibilities for metal-related trash has become increasingly important. In this research, calcium oxide and mixture of calcium, iron, and magnesium oxides was extracted from the wastes of cement factories using hydrofluoric acid. As a result, this research provides a comprehensive picture of waste recycling, and reuse throughout extraction and it examines the current state and potential developments in mineral and metal waste recycling and reusing them in different applications, among these applications, it is used CaO and CaO:MgO:Fe₂O₃ NPs in medical applications, including uterine cancer. Characterizations of the extracted nano-products were done using (XRD) which confirmed the crystalline nature of CaO and the mixture of CaO:MgO:Fe₂O₃ NPs. More, (FESEM) has been used to demonstrate the morphology of the nanostructures of CaO and the mixture CaO:MgO:Fe₂O₃ NPs. The data yielded the average grain size of CaO and the mixture CaO:MgO:Fe₂O₃ NPs calculated by SEM and XRD (64.08, 84.2) nm and (38.636, 31.597) nm respectively. (EDS) spectrum and XRD pattern suggested that prepared CaO and the mixed CaO:MgO:Fe₂O₃ NPs were highly pure. In addition, the ability of NPs as a promising anticancer agent was tested against MES-SA cells line, according to the MTT assay results of MES-SA cells the I_{C50} (91.65 and 98.4) µg/mL for CaO and CaO:MgO:Fe₂O₃ NPs respectively. The results showed that the extracted nanoparticles CaO and the mixture CaO:MgO:Fe₂O₃ NPs served as an anti-cancer agent.

Keywords: CaO and CaO:MgO:Fe₂O₃ NPs, Structure, morphological, Uterus cancer

Introduction

Resource depletion, along with the difficulty of discovering new metal supplies, might have major consequences for world economic growth. Meanwhile, huge volumes of mineral and metal waste with potential economic worth continue to accumulate on the planet's surface as garbage. If these wastes

can be recycled and reused effectively, not only will the exploitation of virgin primary mineral resources be reduced, but it will also lead to the utilization of abandoned minerals and metallic waste, which would otherwise be an environmental hazard. There have been many advancements in the field of mineral and metallic waste recycling and reuse in recent years; thus, the primary goal of this paper is to provide a useful

reference for engineers and researchers in industry and academia on the current state and future trends in mineral and metallic waste recycling and reuse.

Waste arises in many different forms and its characterization can be expressed in several forms. Some common characteristics used in the classification of waste includes the physical states, physical properties, reusable potentials, biodegradable potentials, source of production and the degree of environmental impact. White et al. stated that waste can be classified broadly into three main types according to their physical states; these are liquid, solid and gaseous waste. The most common resource are: Household/Domestic waste, industrial, agricultural waste, commercial waste, demolition, and construction waste in addition to mining waste. The environmental impact of these wastes can cause hazardous waste and non-hazardous waste [1].

Nanomaterials have garnered considerable interest due to their unique qualities of high reaction activity and expansive surface area. These nano-materials with a size range of (1–100 nm) have a greater power to kill up to 650 etiological germs of diverse illnesses than antibiotics, which kill six. Small nanoparticles (NPs) have size dimensions close to the atomic level, resulting in large surface-to-volume ratios that alter physical and chemical properties such as mechanical, biological, melting point, catalytic activity, thermal and electrical conductivities, and optical absorption in comparison to bulk chemical composition. Stable antibacterial agents are composed of inorganic materials at high pressures/temperatures to withstand severe processing conditions compared to organic antibacterial agents and are regarded as safe for use on animals and humans [2].

Nanoparticles are much more active than larger-sized particles because of their much higher surface area. They also exhibit unique physical and chemical properties [2].

Several types of metal and metal oxide nanoparticles such as silver (Ag), silver oxide (Ag_2O), titanium dioxide (TiO_2), zinc oxide (ZnO), gold (Au), calcium oxide (CaO), silica (Si), copper oxide (CuO), and magnesium oxide (MgO) have been known to show antimicrobial activity [3]. Metal or metal ions are also essential elements for human body and play a role in over 300 enzyme reactions in the body [4].

Many researchers tried to use the nanotechnologies throughout various applications like: industrial,

medical agriculture ect. here in this project would focus on the medical and agriculture applications.

Cancer is a disorder that results from genetic or epigenetic alterations in the somatic cells and has abnormal cell growth which may be spread to other body parts. They form a subset of neoplasm. The unregulated growth of cells in a group called neoplasm or tumor and form a lump or mass and may be distributed diffusely [5] uterine cancer: is the most common kind of cancer affecting the female reproductive system.

Cancer of the uterus occurs when cells in any part of the uterus become abnormal, grow out of control and form a lump called a tumour. Cancer of the uterus can be either endometrial cancer or the less common uterine sarcoma.

Uterine cancer has two primary types that develop in different parts of the uterus:

Endometrial cancer: The most common form of uterine cancer. Because the endometrium is part of the uterus, endometrial cancer is often referred to as uterine cancer. Endometrial cancer is the most commonly diagnosed gynecologic cancer (which includes cancers of the uterus, cervix, ovaries, vulva, vagina and fallopian tubes).

More than 80 percent of all endometrial cancers are adenocarcinomas of the endometrium. This type of cancer forms when cells in the endometrium — the inner lining of the uterus — begin to grow out of control. Endometroid carcinoma accounts for most cases of endometrial adenocarcinoma.

Uterine sarcoma: A rarer type of uterine cancer that forms in the muscles or other tissues of the uterus [6-8].

The aim of the research is to extract metal oxides from cement waste and use them in medical applications, including the treatment of uterine cancer.

Experimental

Materials

Cement factory waste obtained from Kufa cement factory, Iraq, hydrofluoric acid (HF) was purchased from Sigma, USA.

Preparation of CaO and $\text{CaO:MgO:Fe}_2\text{O}_3$ NPs

Calcium was extracted from cement waste using hydrofluoric acid at a concentration of 48%, where a quantity of cement waste was placed in a plastic container, and hydrofluoric acid was added three times the amount of waste and left for 12 hours, then

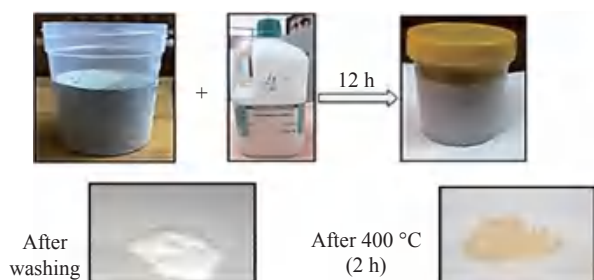


Fig. 1 Steps of preparation process of CaO and CaO:MgO:Fe₂O₃ Nps from cement waste factory.

the mixture was washed with distilled water well more than ten times and left to dry where it got white powder with calcium element. Then the calcium was oxidized to obtain calcium oxide by placing it in the oven at a temperature of 400 °C for 5 hours. As for the mixture of calcium oxide, magnesium oxide and iron oxide, it was obtained from cement waste by heating the powder obtained 12 hours after placing the waste in hydrofluoric acid in the oven for two hours at a temperature of 400 °C. Then the mixture of calcium, magnesium and iron was oxidized to obtain by placing it in the oven at a temperature of 400 °C for 5 hours.

Characterization of CaO and CaO:MgO:Fe₂O₃ Nps

A number of examinations were carried out, including (XRD) was used SHIMADZU X-Ray diffractometer system (XRD-6000) which record the intensity as a function of Bragg's angle. The measurement settings are as follows Target: CuK α Wavelength = 1.506 Ao, Current = 30 mA, Voltage = 40 kV In the range of (20°-80°) with speed 10 (degree/min) with preset time = 0.30 (sec), the scanning angle 2 shifted.

Scanning electron microscopy was used to analyze agglomerations and other properties of the products, the samples have been examined by FESEM (EBSD Instrument: ZEISS SIGMA VP). Fourier transform infrared spectra are generated by the absorption of electromagnetic radiation in the frequency range (400 to 4000 cm⁻¹). The frequency and intensity of absorption are the indications of the band structures and structural geometry of the molecule, as measured by Thermo Fisher Scientific Corporation's FT-IR at Daypetronic Co. in Tehran, Iran.

Maintenance of cell cultures

MES-SA Cells were maintained in RPMI-1640 supplemented with 10% fetal bovine serum, 100 units/mL penicillin, and 100 μ g/mL streptomycin.

Cells were passaged using Trypsin-EDTA reseeded at 80% confluence twice a week, and incubated at 37 °C [9, 10].

MTT assay

To determine the cytotoxic effect of prepared nanoparticles, the MTT assay was done using 96-well plates [11, 12]. Cell line were seeded at 1 \times 10⁴ cells/well. After 24 hrs or a confluent monolayer was achieved; cells were treated with prepared NPs. Cell viability was measured after 24, 48, and 72 hrs of treatment by removing the medium, adding 28 μ L of 2 mg/mL solution of MTT and incubating the cells for 2.5 h at 37 °C. After removing the MTT solution, the crystals remaining in the wells were solubilized by the addition of 50 μ L of DMSO (Dimethyl Sulphoxide) followed by 37 °C incubation for 15 min with shaking [13]. The absorbency was determined on a microplate reader at 492 nm; the assay was performed in triplicate. The inhibition rate of cell growth (the percentage of cytotoxicity) was calculated as the following equation [14]:

$$\text{Inhibition rate \%} = (A - B/A) \times 100 \quad (1)$$

where A is the optical density of control, and B is the optical density of the samples.

Statistical analysis

The obtained data were statically analyzed using an unpaired t-test with Graph Pad Prism [15]. The values were presented as the mean \pm SD of triplicate measurements [16].

Migration assay

Doubling times for cancer cell lines were estimated by plating a known number of cells and measuring the total number of cells once the culture reached an estimated 80% confluency. Proliferation rates were then calculated using the doubling time measurements. Cell line migration was estimated in 43 cancer cell lines using a live cell imaging-based random cell migration assay. The mean speed of cell migration was then quantified as the final migration estimate.

Western blot analysis

Cells were rinsed with phosphate-buffered saline (PBS) before being scraped and lysed in radioimmunoprecipitation assay (RIPA) buffer supplemented with protease inhibitor cocktail and phosphatase inhibitor cocktail II. After centrifugation at 14000 rpm for 15 min, the supernatant fractions were harvested as the total cellular protein extracts. The

protein concentration was determined using a protein assay kit (Solar bio Life Science, Beijing, China). The total cellular protein extracts were separated by sodium dodecyl sulfate polyacrylamide gel electrophoresis (SDS-PAGE) and transferred to polyvinylidene fluoride membranes in 20 mM Tris-HCl (pH 8.0), 150 mM glycine, and 20% (v/v) methanol. Membranes were blocked with 5% nonfat dry milk in 1xPBS containing 0.05% Tween-20 (PBS-T) and incubated with antibodies against p-TOPK, TOPK, p-ERK1/2, ERK1/2, p-RSK2, RSK2, p-c-Jun, total c-Jun, PARP, caspase 3, caspase 7, cleaved PARP, cleaved caspase 3, cleaved caspase 7, or β -actin at 4°C, overnight. Blots were washed three times with 1xPBS-T buffer, followed by incubation with the appropriate horseradish peroxidase-linked immunoglobulin G (IgG). The specific proteins in the blots were visualized using an enhanced chemiluminescence detection reagent and the Amersham Imager 600 (GE Healthcare life Science, Pittsburgh, PA, United States).

Results and Discussion

X-ray diffraction (XRD) of CaO and CaO:MgO:Fe₂O₃ NPs

The X-ray diffraction patterns of CaO and the mixture nanostructure CaO:MgO:Fe₂O₃ NPs are shown in Fig. 2 respectively. All XRD patterns reveal the polycrystalline nature of prepared samples.

Table 1 illustrates bragg's angles, Full width at half-maximum, grain size and miller indices of CaO and the mixed sample CaO:MgO:Fe₂O₃ NPs. From Fig. 2(a) can observe the corresponding of CaO NPs, it can be observed that the dominant phase was cubic with preferential orientation along (111) at 32.52°. Also, it can be observed the existence of two peaks along (200) and (220), (222) at 37.32, 53.68, 68.64, this data was confirmed by the ASTM (37-1497) card of CaO. Our results are correlated with other researches [17, 18] while, (220) at 47.02 has good agreement with [19].

The mixed sample CaO:MgO:Fe₂O₃ NPs which is

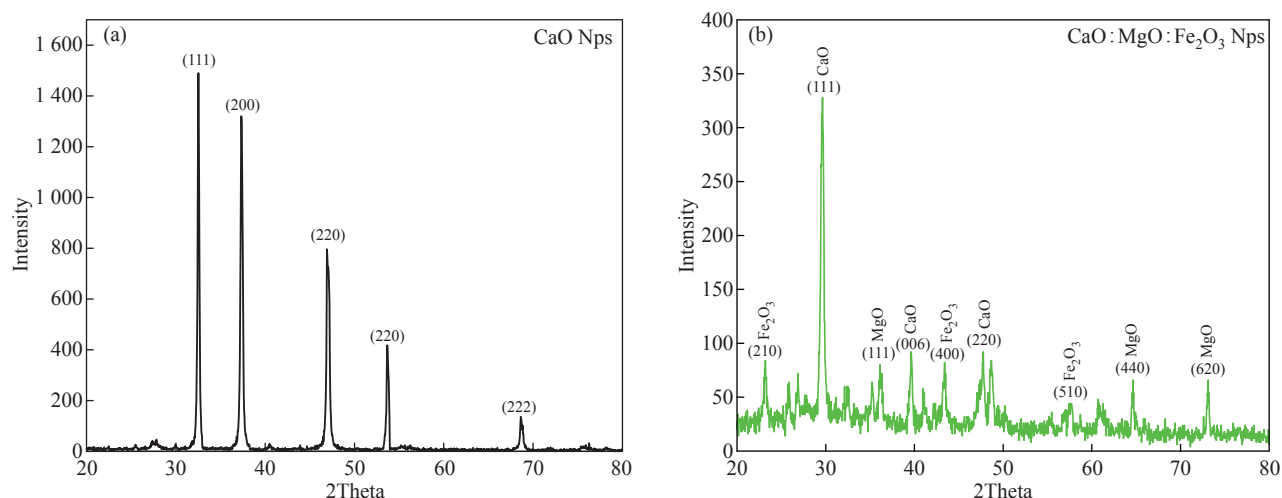


Fig. 2 XRD patterns of (a) CaO Nps and (b) CaO:MgO:Fe₂O₃ NPs.

Table 1 The obtained result of the XRD for CaO NPs and CaO:MgO:Fe₂O₃ NPs

Sample	2 θ stand (deg.)	2 θ Exp. (deg.)	FWHM (rad)	Miller indices (h k l)	D (nm)	Avg. D (nm)
CaO	32.203	32.52	0.004155	(111)	34.756	38.636
	37.346	37.32	0.003885	(200)	37.668	
	47.568	47.02	0.003846	(220)	39.292	
	53.854	53.68	0.003844	(220)	40.415	
	67.373	68.64	0.004091	(222)	41.051	
CaO:MgO:Fe ₂ O ₃	29.756	30.04	0.007073	(111)	20.277	31.597
	36.936	36.12	0.007435	(111)	19.615	
	39.276	39.6	0.005658	(006)	26.043	
	43.284	43.36	0.007010	(400)	21.282	
	47.568	47.68	0.006213	(220)	24.397	
	56.106	56.88	0.002792	(510)	56.478	
	64.526	64.56	0.004653	(440)	35.248	
73.327	73.04	0.003490	(620)	49.436		

illustrated in Fig. 2(b) has a dominated phase for all peaks and matches with the ASTM card of CaO:MgO:Fe₂O₃ NPs with preferential orientation along (111) at 29.64° the resultant correlates with research [20]. The crystallite size has been estimated from the XRD pattern using Scherer's Equation (2):

$$D = 0.9\lambda/\beta\cos\theta \quad (2)$$

where λ is the X-ray wavelength of Cu K α Radiation (1.54 Å), θ is the Bragg diffraction angle, and β is the FWHM of the discrete diffraction peak. The crystal size average was found to be 38.636, 31.597 nm of CaO and CaO:MgO:Fe₂O₃ NPs respectively.

Field Emission Scanning Electron Microscope

Figure 3 shows the Energy dispersive X-ray for cement waste, observed from the figure that the waste contains many elements calcium, silicon, chlorine, potassium, iron, sulfur, magnesium, carbon, oxygen and aluminum. Calcium was the highest percentage among the elements, followed by silicon, sulfur, potassium and the rest of the elements.

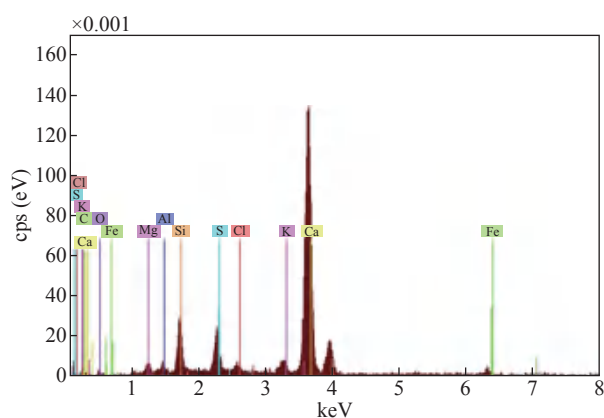


Fig. 3 Energy Dispersive X-ray (EDX) of the cement waste.

Figure 4 shows the Ca and Ca:Mg:Fe extracted from cement waste.

Figure 5 shows the SEM and EDX Images of CaO NPs and CaO:MgO:Fe₂O₃ NPs. CaO and CaO:MgO:Fe₂O₃ NPs synthesized by extraction method using HF acid to obtain calcium oxide and the mixture. Figure 5(a) shows that the grain size CaO NPs were well dispersed with ranging between (48.77-87.57) nm. At the lab field, synthesized the CaO NPs were agglomerated (the particles have more tendency to agglomeration. Enhanced surface to volume ratio in nanoparticles is the reason) and formed larger clusters [9, 11]. Figure 5(b) shows that the size

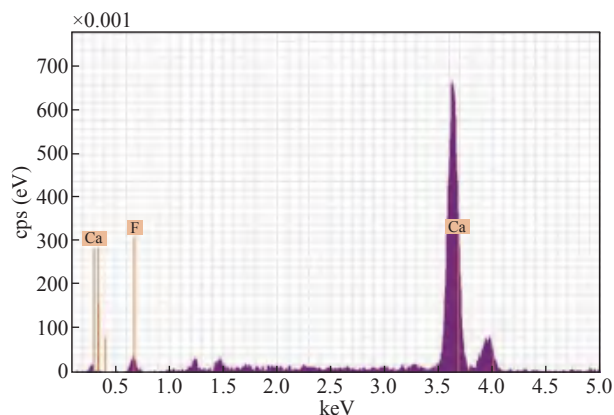


Fig. 4 Energy Dispersive X-ray (EDX) of the cement waste after adding hydrofluoric acid.

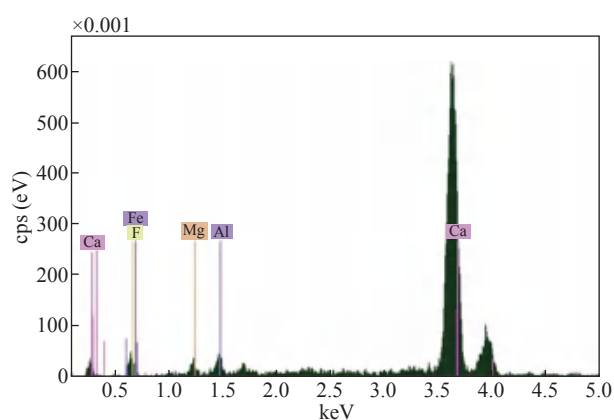


Fig. 5 Energy Dispersive X-ray (EDX) of the cement waste after adding hydrofluoric acid and the heat treatment.

of CaO:MgO:Fe₂O₃ NPs, the grain size is ranging between (81.19-88) nm. To determine the proportions of elements in compounds, energy-dispersive X-ray analysis is used.

In this study, it was used to show the presence of CaO NPs, and the mixed sample CaO:MgO:Fe₂O₃ NPs in a certain proportion. The analyzed were reported in different patterns as shown in Fig. 6(a) for CaO NPs and 6(b) for CaO:MgO:Fe₂O₃ NPs under the EDX spectrum of the study. Further, Fig. 6(a) reflects the presence of Calcium and oxygen with a weight ratio of 89.9% and 10.1%. Similarly, and Fig. 6(b) records the presence of Calcium, magnesium, Iron, and oxygen with a weight ratio of 65%, 2%, 23%, and 9.9% respectively.

UV-VIS properties of CaO NPs and the mixture of CaO:MgO:Fe₂O₃ NPs

The optical properties of the CaO and the mixture of CaO:MgO:Fe₂O₃ NPs are determined from the Absorbance (A), measurements were in the range 200–900 nm. Figure 7 displays the variation of

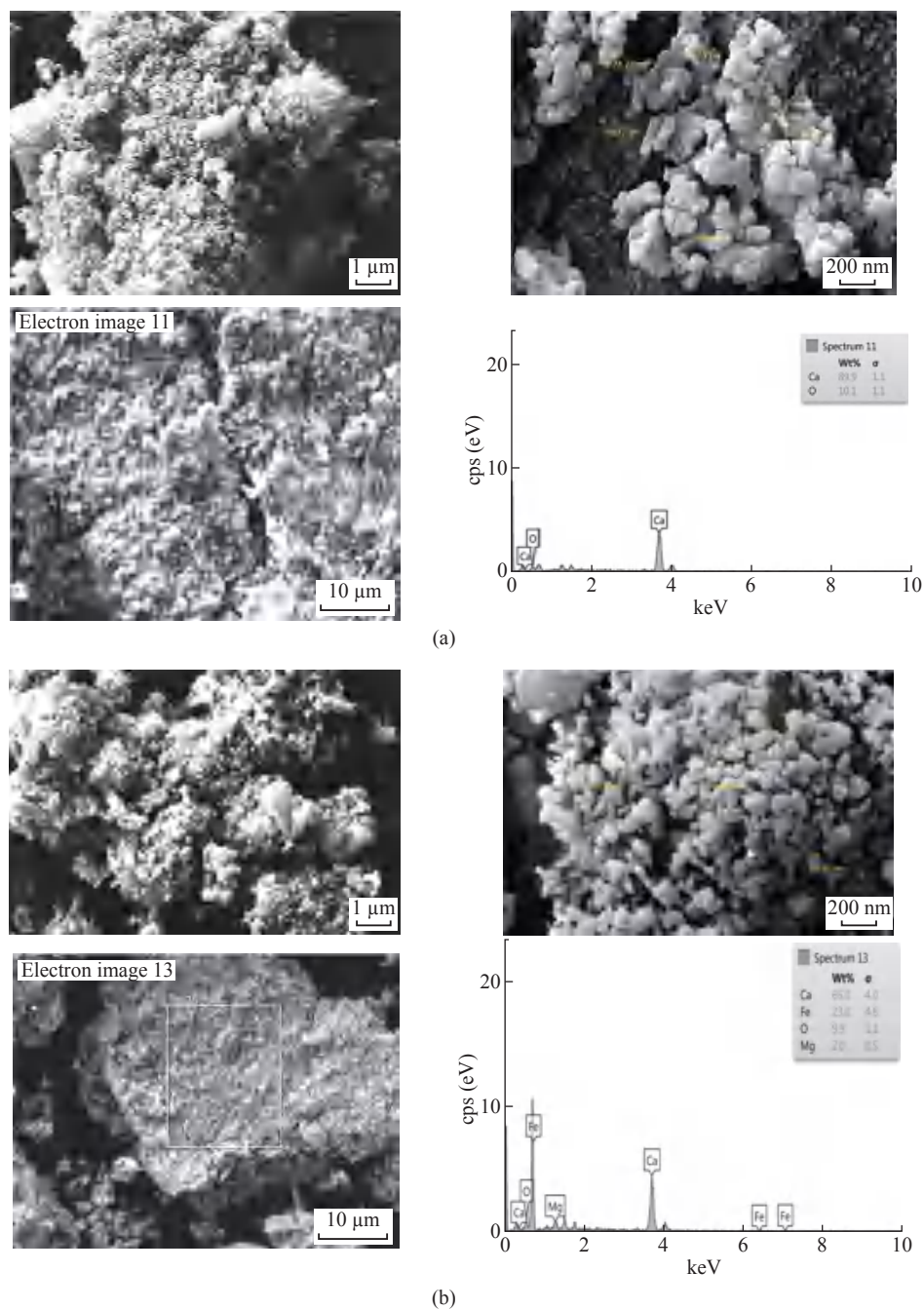


Fig. 6 FE-SEM images of (a) CaO and (b) CaO:MgO:Fe₂O₃ NPs.

absorbance spectra with wavelength from (200 to 900) nm of the CaO and the mixture of CaO:MgO:Fe₂O₃ NPs. It appeared that CaO and MgO: Fe₂O₃ have high absorbance in the visible region, indicating its applicability as an absorbing material [21].

Fourier transform infrared spectroscopy (FTIR) analysis

Fourier transform infrared (FTIR) spectroscopy is an important tool for observation of functional groups, it was employed in this work to characterize the different

functional groups, which are involved in the reduction of the stabilization of prepared CaO and the mixed sample of CaO:MgO:Fe₂O₃ NPs powders. The FTIR spectrum for CaO is shown in Fig. 8(a). FTIR analysis expressed visible bands at 3452.23, 1173.43, 1123.89, 738.78, and 638.45 cm⁻¹. The band found at 3452.23 cm⁻¹ can be assigned to stretching of the O-H [10]. The two peaks appeared between 1173.43-1123.89 cm⁻¹ which refers to C-O stretching vibration [1810-2214]. The peaks appear 638.45 cm⁻¹ refers to C-H out of plane bending, strong band observed at 718.78 cm⁻¹ is due to the (Ca-O) bond, and it is consistent with

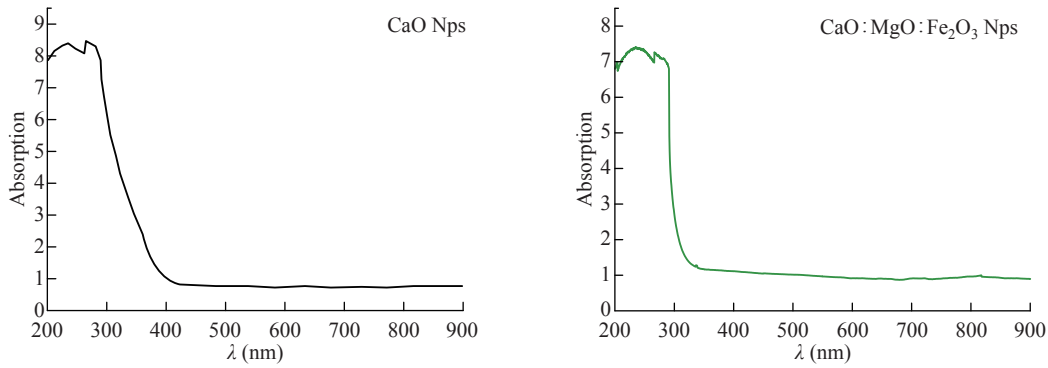


Fig. 7 Absorbance spectrums of CaO and CaO:MgO:Fe₂O₃ NPs

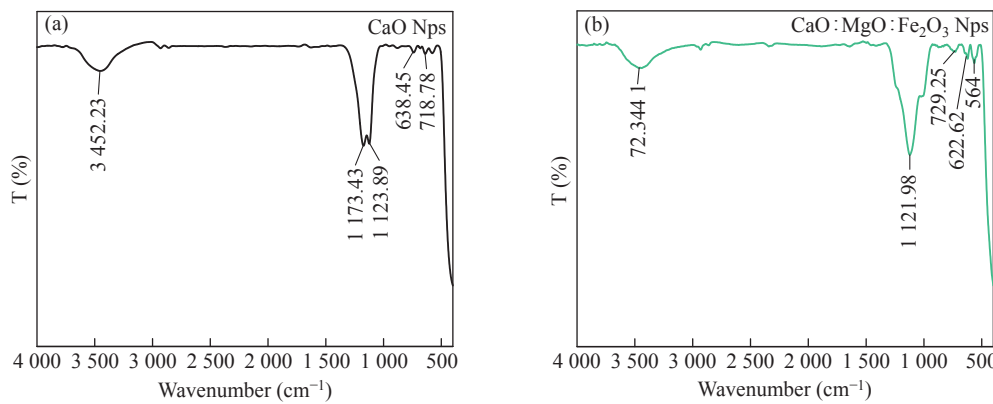


Fig. 8 Fourier transforms Infrared (FT-IR) analysis of (a) CaO and (b) CaO:MgO:Fe₂O₃ NPs.

literature values [23, 24].

Figure 8(b) shows the FTIR spectrum of the synthesized mixture of CaO:MgO:Fe₂O₃ NPs the band found at 3441.72 cm⁻¹ can be assigned to stretching of the O-H. 1121.98 cm⁻¹ refer to C-O stretching vibration. The peaks appear between 729.25 and 622.62 cm⁻¹ refers to C-H out of plane bending 564 cm⁻¹.

Cell viability (MTT Assay)

To check the cytotoxicity of the individual samples of CaO and the mixed sample of CaO:MgO:Fe₂O₃ NPs on the MES-SA (1×10⁵ mL⁻¹) cells per well in their exponential growth phase, they were incubated

with increasing of the CaO and the mixture of CaO:MgO:Fe₂O₃ NPs concentrations for 24 hours, and the cell viability was expressed as a percentage of the untreated control (100% cell viability was investigated by MTT assay). Cytotoxicity results of MES-SA cell viability after 72 hours of treatment with various concentrations of each CaO NPs and the mixture of CaO:MgO:Fe₂O₃ NPs (6.25 to 400 μg/mL) are shown in Fig. 9. All results indicated that, a decrease in cell viability in a dose-dependent manner, and both CaO NPs, and the mixture of CaO:MgO:Fe₂O₃ NPs solutions resulted in a significant decrease in the survival rate of MES-SA cells in dose dependence (*P* < 0.0001). For CaO NPs at a concentration of (6.25 and 12.5

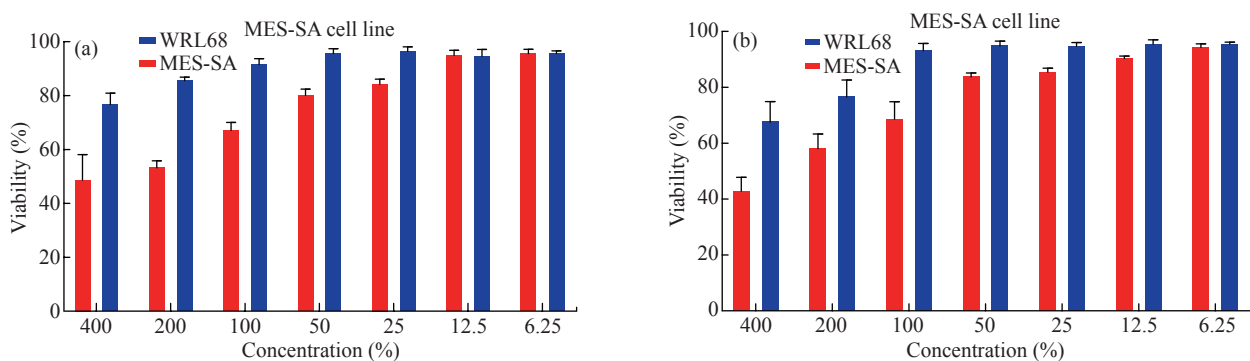


Fig. 9 Cell Viability rate of syntheses (a) CaO, (b) CaO:MgO:Fe₂O₃ NPs MES-SA cell line.

Table 2 Viability (mean \pm standard deviation (SD) of syntheses CaO NPs

Concen. ($\mu\text{g/mL}$)	MES-SA		WRL68	
	Mean	\pm SD	Mean	\pm SD
400	49.16	8.97	77.28	3.65
200	53.70	2.12	86.03	0.85
100	67.62	2.41	92.13	1.56
50	80.59	1.80	96.18	1.25
25	84.79	1.33	96.95	1.14
12.5	95.41	1.41	94.91	2.20
6.25	96.14	1.05	96.10	0.48

Table 3 Viability (mean \pm standard deviation (SD) of syntheses CaO:MgO:Fe₂O₃ NPs

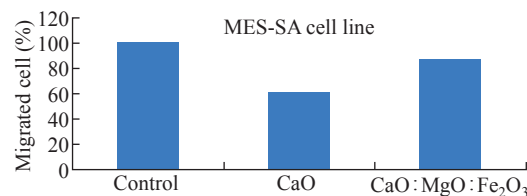
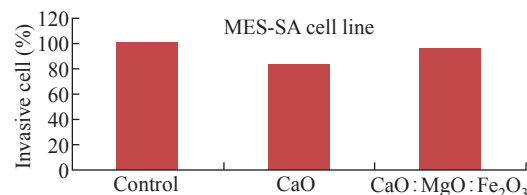
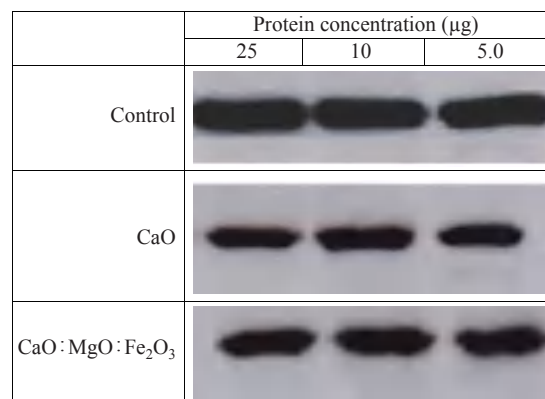
Concen ($\mu\text{g/mL}$)	MES-SA		WRL68	
	Mean	\pm SD	Mean	\pm SD
400	43.38	4.42	68.09	6.80
200	58.60	4.70	77.08	5.52
100	69.11	5.75	93.60	2.10
50	84.29	0.82	95.33	1.18
25	85.95	0.90	95.22	0.82
12.5	90.87	0.29	95.95	1.03
6.25	94.83	0.71	95.95	0.20

$\mu\text{g/mL}$), there was no significant difference between MES-SA carcinoma and normal cell WRL68, but there are significant differences at higher concentrations of (100, 200, 400 $\mu\text{g/mL}$). At concentrations (6.25 to 50 $\mu\text{g/mL}$), we found that the viability rate of the normal cell WRL68 remained nearly unchanged at 96.10, 96.18%, whereas the viability rate of the MES-SA carcinoma decreased to 53.70 at concentrations (200 $\mu\text{g/mL}$). And a 49.16 cell death rate at the highest concentration (400 $\mu\text{g/mL}$), while the I_{C50} was (91.65 $\mu\text{g/mL}$) for MES-SA and normal cell WRL68 was significantly higher (231.2 $\mu\text{g/mL}$). Table 2 show viability (mean \pm standard deviation (SD) of syntheses CaO NPs.

The cytotoxicity results of the mixture of CaO:MgO:Fe₂O₃ NPs are shown in Fig. 9(b) and Table 3. Cell viability loss was observed, which was dose-dependent. At a concentration of 25 g/mL for the mixture of CaO:MgO:Fe₂O₃ NPs, there is no significant difference between MES-SA carcinoma and normal cell WRL68. At higher concentrations (200 and 400 $\mu\text{g/mL}$) they observed a significant difference. The normal cell WRL68 viability rate was 77.08, 68.09, whereas the MES-SA carcinoma viability rate was 58.60, 43.38.13%. The I_{C50} was (98.4 $\mu\text{g/mL}$) for MES-SA and normal cell WRL68 was significantly higher (173.3 $\mu\text{g/mL}$) for the mixture of CaO:MgO:Fe₂O₃ NPs. Table 3 shows the viability (mean \pm standard deviation (SD) of syntheses the mixture of CaO:MgO:Fe₂O₃ NPs.

The migrated and invasive MES-SA cell rate was reduced after CaONPs, and CaO:MgO:Fe₂O₃ NPs

treatment, as shown in Figs. 10 and 11. In Fig. 10 the migrated cell rate decreased when compared to the

**Fig. 10** CaONPs and CaO:MgO:Fe₂O₃ NPs inhibited the migration of MES-SA cells.**Fig. 11** CaO NPs and CaO:MgO:Fe₂O₃ NPs inhibited the invasion of MES-SA cells.**Fig. 12** Western blot of CaO and CaO:MgO:Fe₂O₃ Nps.

control group for CaO NPs 60% treatment, and 86% with CaO:MgO:Fe₂O₃ NPs treatment. Also, It can be observed that the invasive cell rate decreased to 70% of the control group for CaO NPs treatment, and 92% with CaO:MgO:Fe₂O₃ NPs treatment. Western blot analysis was used for protein expression analysis, and total protein was extracted according to the manufacturer's protocol for MES-SA cell movement and invasion rate measurements Fig. 12.

Conclusions

To our knowledge, the present study is the first to show the anticancer of the extracted CaO and CaO:MgO:Fe₂O₃ NPs. CaO and CaO:MgO:Fe₂O₃ NPs was extracted from the wastes of cement factories using hydrofluoric acid with a concentration of 48%. X-ray diffraction pattern (XRD) showed the crystalline nature of CaO and CaO:MgO:Fe₂O₃ NPs. FTIR measurements also validated the purity of CaO and CaO:MgO:Fe₂O₃ NPs. The anticancer effect of CaO and CaO:MgO:Fe₂O₃ NPs against MES-SA cell line was examined. The findings CaONPs and CaO:MgO:Fe₂O₃ NPs good inhibition for the MES-SA cell. According to the MTT assay results of MES-SA cells the I_{C50} (91.65 and 98.4) µg/mL for CaO and CaO:MgO:Fe₂O₃ NPs respectively, there is little difference in IC₅₀ of CaO:MgO:Fe₂O₃ NPs in comparison to CaO. Because according to the results of edx, the highest percentage in the mixture is calcium, so the ic₅₀ values are close. In the future, the formed CaO and CaO:MgO:Fe₂O₃ NPs could be applied in biomedical applications as an anticancer new agent.

Conflict of Interests

The authors declare that no competing interest exists.

References

- [1] Ebikapade Amasuomo & Jim Baird, The Concept of Waste and Waste Management, Journal of Management and Sustainability; Vol. 6, No. 4; 2016: 88-96.
- [2] A. Haider, M. Ijaz, M. Imran, M. Naz, H. Majeed, J.A. Khan, M.M. Ali, M. Ikram, Enhanced bactericidal action and dye degradation of spicy roots' extract-incorporated ne-tuned metal oxide nanoparticles, Applied Nanoscience (2019), 10(2):3.
- [3] Dizaj S.M., Mennati A., Jafari S., Khezri K., Adibkia K. Antimicrobial activity of carbon-based nanoparticles. Advanced pharmaceutical bulletin. 2015; 5(1): 19.
- [4] Mahboubeh Mirhosseini, Synergistic Antibacterial Effect

- of Metal Oxid Nanoparticles and Ultrasound Stimulation, J. Biol. Today's World. 2015 June; 4(6): 138-144
- [5] Anupam Saini, Manish Kumar, Shailendra Bhatt, Vipin Saini and Anuj Malik, CANCER CAUSES AND TREATMENTS, IJPSR (2020), Volume 11, Issue 7.
- [6] American Society of Clinical Oncology. *Uterine Cancer*. 2014: <http://www.cancer.net/cancer-types/uterine-cancer/view-all>
- [8] Nancy Innocentia Ebu, Sylvia C Mupepi, Mate Peter Siakwa, Carolyn M Sampselle, Knowledge, practice, and barriers toward cervical cancer screening in Elmina, Southern Ghana, Int J Womens Health. 2015; 7: 31-39.
- [9] Frederic Amant, Philippe Moerman, Patrick Neven, Dirk Timmerman, Erik Van Limbergen, Ignace Vergote Endometrial cancer 2005 Aug 6-12; 366(9484): 491-505. doi: 10.1016/S0140-6736(05)67063-8. PMID: 16084259.
- [10] Al-Ziaydi, A.G., Al-Shammari, A.M., Hamzah, M.I., and Jabir, M.S. (2020). Hexokinase inhibition using D-Mannoheptulose enhances oncolytic newcastle disease virus-mediated killing of breast cancer cells. Cancer Cell International, 20(1): 1-10.
- [11] Al-Ziaydi, A.G., Hamzah, M.I., Al-Shammari, A.M., Kadhim, H.S., and Jabir, M.S. (2020, December). The anti-proliferative activity of D-mannoheptulose against breast cancer cell line through glycolysis inhibition. In AIP Conference Proceedings (Vol. 2307, No. 1, 020023). AIP Publishing LLC.
- [12] Al Salman, H.N.K., Ali, E.T., Jabir, M., Sulaiman, G.M., and Al Jadaan, S.A. (2020). 2 Benzhydrylsulfinyl N hydroxyacetamide Na extracted from fig as a novel cytotoxic and apoptosis inducer in SKOV 3 and AMJ 13 cell lines via P53 and caspase 8 pathway. European food research and technology.
- [13] Al-Ziaydi, A.G., Al-Shammari, A.M., Hamzah, M.I., Kadhim, H.S., and Jabir, M.S. (2020). Newcastle disease virus suppress glycolysis pathway and induce breast cancer cells death. VirusDisease, 1-8.
- [14] Jabir, M.S., Hussien, A.A., Sulaiman, G.M., et al., Green synthesis of silver nanoparticles from Eriobotrya japonica extract: a promising approach against cancer cells proliferation, inflammation, allergic disorders and phagocytosis induction. Artificial Cells, Nanomedicine, and Biotechnology, 2021, 49(1), 48-60.
- [15] Al-Shammari, A.M., Al-Saadi, H., Al-Shammari, S.M., and Jabir, M.S. (2020). Galangin enhances gold nanoparticles as anti-tumor agents against ovarian cancer cells. In AIP Conference Proceedings (Vol. 2213, No. 1, p. 020206). AIP Publishing LLC.
- [16] Khashan, K.S., Abdulameer, F.A., Jabir, M.S., Hadi, A.A., and Sulaiman, G.M. (2020). Anticancer activity and toxicity of carbon nanoparticles produced by pulsed laser ablation of graphite in water. Advances in Natural Sciences: Nanoscience and Nanotechnology, 11(3), 035010.
- [17] Sameen, A.M., Jabir, M.S., and Al-Ani, M. Q. (2020). Therapeutic combination of gold nanoparticles and LPS as cytotoxic and apoptosis inducer in breast cancer cells. In AIP Conference Proceedings (Vol. 2213, No. 1, p. 020215). AIP Publishing LLC.
- [18] Suresh Kumar, Vandana Sharma, Jatindra Kumar Pradhan, Sanjay Kumar Sharma, Prem Singh, Jatinder Kumar Sharma, Structural Optical and Antibacterial Response of CaO Nanoparticles Synthesized via Direct Precipitation Technique, Nano Biomed. Eng., 2021, Vol. 13, Iss. 2, 172-178.
- [19] Zahra Mirghiasi, Fereshteh Bakhtiari, Esmaeel Darezereshki, Esmat Esmaeilzadeh, Preparation and characterization of CaO nanoparticles from Ca(OH)₂ by direct thermal decomposition method, Journal of

- Industrial and Engineering Chemistry, 20(2014): 113-117.
- [20] A.S. Balaganesh, R. Sengodan, R. Ranjithkumar, B. Chandarshekar Synthesis and Characterization of Porous Calcium Oxide Nanoparticles CaO N International Journal of Innovative Technology and Exploring Engineering(IJITEE) ISSN: 2278-3075, Volume-8, Issue-2S, December, 2018: 312-314.
- [21] Wisam Okash Toamah, Ayad Kadhim Fadhil, Preparation of nanoparticles from CaO and use it for removal of chromium (II), and mercury (II) from aqueous solutions, IOP Conf. Series: Journal of Physics: Conf. Series1234 (2019) 012086. doi:10.1088/1742-6596/1234/1/012086(1-9).
- [22] B. Bhardwaj, Nanotechnology: Various methods used for preparation of Nanomaterials, p. 386, 2019, doi: 10.31024/ajpp.2018.4.4.2.
- [23] A. Dhupar, S. Kumar, V. Sharma, Mixed structure Zn(S,O) nanoparticles: Synthesis and characterization. *Materials Science Poland*, 2019, 37: 230-237.
- [24] Keene Carlvin Mmusi, Sebusi Odisitse, Florence Nareetsile, Comparison of CaO-NPs and Chicken Eggshell-DerivedCaOin the Production of Biodiesel from (Mongongo) Nut Oil, *Hindawi Journal of Chemistry*, Volume 2021, Article ID 6663722, 15.
- [25] Reta G. Jalu , Tariku A. Chamada, Dr. Ramachandran Kasirajanc, Calcium oxide nanoparticles synthesis from hen eggshells for removal of lead (Pb (II)) from aqueous solution *Environmental Challenges*, Volume 4, August 2021, 100193.

Copyright© Nadia Jasim Ghdeeb, Asmaa Hadi Mohammed, and Aseel Mustafa Abdul Majeed. This is an open-access article distributed under the terms of the Creative Commons Attribution License, which permits unrestricted use, distribution, and reproduction in any medium, provided the original author and source are credited.